PAPER

CrossMark
← click for updates

Understanding the formation and evolution of interdiffusion grown organolead halide perovskite thin films by thermal annealing†

Cheng Bi,[a] Yuchuan Shao,[a] Yongbo Yuan,[a] Zhengguo Xiao,[a] Chenggong Wang,[b] Yongli Gao[b] and Jinsong Huang*[a]

Organolead trihalide perovskites are emerging excellent active materials for thin film solar cells. Here, the formation and evolution of methylammonium lead iodide perovskite thin films grown by the low-temperature thermal annealing induced interdiffusion process are investigated. It is found that thermal annealing not only drives the formation of perovskite but also affects the morphology, optoelectronic properties and correlated device performance. Thermal annealing at 105 °C quickly drives the formation of phase-pure perovskite in a short time of 15 min, and continued thermal annealing up to two hours continuously increases the perovskite crystallinity and grain size without losing film continuity or coverage. The measured Hall mobility increases monotonically to 36.0 cm^2 V^{-1} s^{-1} upon annealing, which is correlated with the increased crystallinity and grain size. Device efficiencies increase with an increased short circuit current density and fill factor with a longer annealing time up to two hours, and the highest device efficiency of 13.4% is achieved. It is found that the reduction of work function in the perovskite films, caused by the increased annealing duration, is linearly correlated with the open circuit voltage loss, which points out a path for the further increase of the device efficiency.

1. Introduction

Solar energy is a reliable, renewable and clean resource in contrast to conventional fossil fuels. Thin film photovoltaic devices, with features like low cost, light weight, and easy fabrication, are promising for solar energy harvesting.[1–3] One effective way to reduce the cost of photovoltaic devices is to increase their efficiencies.[3] Thermal annealing is broadly applied in both organic and inorganic thin film solar cells to improve device performance.[4–11] In organic solar cells, thermal annealing was often used to increase the crystallinity of polymers and to form the optimized polymer/fullerene domain sizes for charge generation in polymer solar cells.[4,6,12–14] In inorganic thin film solar cells, thermal annealing treatment governs the performance of devices by performing versatile functions, such as facilitating the incorporation of alkali into the polycrystalline Cu(In, Ga)Se$_2$ (CIGS) thin film for defect passivation,[10,15,16] increasing crystallinity,[17,18] coarsening the crystalline domains,[11,19] and homogenizing the crystal structure in the CIGS active layer.[9,20]

Recently, organolead halide perovskites have been emerging as a new generation of photovoltaic materials for both sensitized solid-state mesoporous structure solar cells and thin film solar cells.[1,21–32] The materials are inexpensive, nature-abundant and solution processable. Efficiency above 15% was achieved by perovskite-based devices with both planar and mesoporous structures after few years of development.[21,23–25,31,32] The mesoporous structure which usually applies TiO$_2$ as an electron conductive layer requires a high-temperature sintering process, and photocatalytic TiO$_2$ increases the risk of deteriorating device stability under UV light.[33] Recent demonstration of a low temperature solution-processed TiO$_2$-free hybrid solar cell employing a perovskite/fullerene bilayer structure as the active layer provides a possibility to produce perovskite photovoltaic devices by using the recently developed large scale, high throughput solution deposition methods for polymer solar cells.[34,35] However the poor perovskite film quality with very rough and non-continuous perovskites leads to a low device efficiency due to the quick crystallization of perovskite from the blended precursor solution.[27] It has been recently realized by the community that there is a strong correlation between the perovskite film quality and the device performance. In one of our recent studies,[36] spin coating of lead iodide (PbI$_2$) and methylammonium iodide (MAI) stacked layers was found to form continuous and pin-hole free perovskite films, as illustrated in Fig. 1. It was found the thermal annealing right after the spin coating of the stacked layers was critical to improve the

^{a}*Department of Mechanical and Materials Engineering, Nebraska Center for Materials and Nanoscience, University of Nebraska-Lincoln, Lincoln, Nebraska 68588-0656, USA*

^{b}*Department of Physics and Astronomy, University of Rochester, Rochester, NY 14627, USA. E-mail: jhuang2@unl.edu*

† Electronic supplementary information (ESI) available: XRD pattern of the perovskite film with 150 °C annealing. See DOI: 10.1039/c4ta04007d
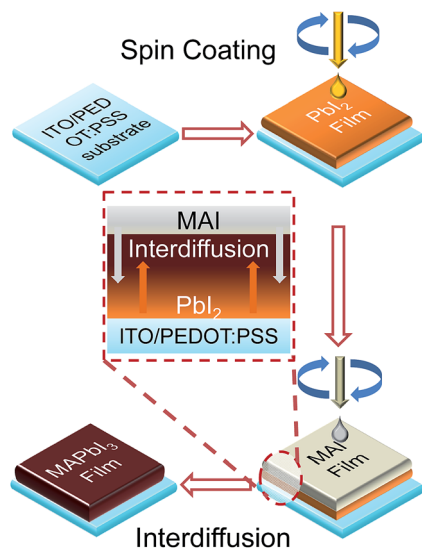
Fig. 1 Schematic illustration of the fabrication procedure of interdiffusion grown perovskite films: the interdiffusion process on the two stacked precursor layers starts after deposition and reaches completeness on further thermal annealing.

device efficiency. One can speculate that the thermal annealing here has two different functions that are different from regular thermal annealing processes: (1) driving the interdiffusion of PbI_2 and MAI precursors for the formation of perovskite and (2) inducing the recrystallization and grain growth in the formed perovskite films. In this manuscript, we report the thermal annealing effect on structural, electrical, and optical properties of methylammonium lead iodide ($MAPbI_3$) perovskite thin films and correlate it with the device performance. We observed a strong influence of thermal annealing on crystallinity and grain size of the perovskite films as well as on the carrier mobility and concentration, correlating well with the device performance.

2. Experimental section

2.1. MAI synthesis

MAI was synthesized by the method reported elsewhere.[37] Typically, hydriodic acid (HI) (15.0 ml, 57 wt% in water, Alfa Aesar) solution was mixed with methylamine (MA) (13.5 ml, 40 wt% in aqueous solution, Alfa Aesar) in an ice bath under stirring for 2 h under the nitrogen atmosphere. The resulting solution was evaporated using a rotary evaporator to remove the solvent. MAI was precipitated during the evaporation process and was purified by washing it three times with diethyl ether. After that, the obtained powder was dried in a vacuum.

2.2. Film formation and device fabrication

PbI_2 and MAI were dissolved in anhydrous dimethylformamide (DMF) and 2-propanol with a concentration of 400 mg ml^{-1} and 40 mg ml^{-1}, respectively. To produce a high performance device, a relatively high concentration of MAI solution was used here. Before the device fabrication, indium tin oxide (ITO) glass substrates have been cleaned with water, acetone and isopropyl

alcohol (IPA). After that, poly(3,4-ethylenedioxythiophene) poly(styrenesulfonate) (PEDOT:PSS) was spin coated on the substrate at a rotation speed of 3000 rpm for 60 s. The 25 nm thick PEDOT film was thermally annealed at 135 °C for 20 min. Hot PbI_2 precursor solution (70 °C) was spin coated on the PEDOT:PSS surface in nitrogen at a rotation speed of 6000 rpm for 45 s, and then the PbI_2 film was dried at 70 °C for 15 min. The MAI solution (room temperature) was spin coated on the top of the PbI_2 film at a rotation speed of 6000 rpm for 35 s. The spin coated MAI layer was dried at 75 °C for 10 min. It is known that a high annealing temperature of above 150 °C can cause quick decomposition of the formed perovskite films (Fig. S1†).[28,38] In our study, in order to avoid significant decomposition, the as-fabricated films were annealed in nitrogen at a relatively low temperature of 105 °C with varied annealing times from 15 min to 3 h.

In order to reduce the surface defects of the perovskite film an additional phenyl-C61-butyric acid methyl ester (PCBM) film was spin coated on top of the formed perovskite layer from a 20 mg ml^{-1} PCBM solution in dichlorobenzene (DCB), as described elsewhere.[36] After that, 20 nm C_{60}, 8 nm 2,9-dimethyl-4,7-diphenyl-1,10-phenanthroline (BCP) and a 100 nm aluminium layer was sequentially deposited on the film by thermal evaporation. The resulting devices have a structure of ITO/PEDOT:PSS (25 nm)/$MAPbI_3$ (280 nm)/PCBM (20 nm)/C_{60} (20 nm)/BCP (8 nm)/Al (100 nm). The working area of these devices is 6 mm^2.

2.3. Film characterization

The single path absorption spectra of the perovskite film were recorded using a Evolution 201 UV-Visible spectrometer (thermo Scientific). X-ray diffraction (XRD) patterns of the film were obtained using a Rigaku D/Max-B X-ray diffractometer with Bragg–Brentano parafocusing geometry. A Co-Kα tube was employed in XRD measurements with a working wavelength of 1.79 Å. The morphology of the film was studied using a Quanta 200 FEG Environmental Scanning Electron Microscope (SEM). The Hall effect and conductivity measurements were conducted in air by using six contacts The Hall bar method, during which the DC current flowing through the perovskite film was applied using a Keithley Model 2400 and the Hall voltage was recorded using a Keithley Model 4200. The validity of the measurement was verified by measuring a standard n-type Si sample with a doping level of 1.8×10^{14} cm^{-3}. The work function of the perovskite films was measured by ultraviolet photoelectron spectroscopy (UPS), which was performed with a VG ESCA Lab system equipped with an ultrahigh vacuum system and a He discharge lamp. The UPS spectra were recorded using an unfiltered He I (21.2 eV) excitation source, and the samples were biased at −5.0 V to observe the low-energy secondary cutoff. The UV light spot size on the sample was about 1 mm in diameter.

2.4. Device characterization

A xenon-lamp-based solar simulator (Oriel 67005, 150 W Solar Simulator) was used to provide simulated AM 1.5 G irradiation (100 mW cm^{-2}). The light intensity was calibrated using a KG5

This journal is © The Royal Society of Chemistry 2014

J. Mater. Chem. A, 2014, 2, 18508–18514 | 18509

colour-filtered Si diode (Hamamatsu S1133). A Keithley Model 2400 was used for the current–voltage measurement. The series resistance was obtained by fitting the current density–voltage (J–V) curves in the bias range of 1.3–1.5 V, and the shunt resistance was obtained by fitting the J–V curves in the bias range of −0.2–0.2 V.

3.   Result and discussion

3.1.   Ultraviolet-visible absorption study

In order to understand the formation and evolution process of the MAPbI$_3$ film during thermal annealing processes, the optical properties of the fabricated films were studied for the first time. As shown in Fig. 2, the film dried at 75 °C for 15 min has broad absorption with the absorption edge around 800 nm, confirming the formation of MAPbI$_3$ right after drying. The absorption in the long wavelength range around 600–800 nm increased gradually in the first hour of annealing, which indicates that the reaction between precursors was not completed right after drying, and thermal annealing is required to drive the interdiffusion of MAI and PbI$_2$ precursors into each other. The absorption remains unchanged after one hour of annealing.

3.2.   X-Ray diffraction study

In order to understand the formation and evolution of perovskite films' phase and crystallization by thermal annealing, XRD measurement of the films has been carried out. Fig. 3(a) shows the XRD patterns of the annealed films with different annealing times. The peaks originating from the MAI (23.13°) and PbI$_2$ (14.96°) phase disappeared after the first 15 min of thermal annealing at 105 °C, confirming the quick reaction between MAI and PbI$_2$ under thermal annealing. The XRD peaks observed at 16.69°, 23.50°, 33.40° and 37.45° are assigned to (110), (112), (220) and (310) crystal planes of the MAPbI$_3$ perovskite structure, which agrees with previous studies using a Cu-Kα radiation source.[23,28,39] No peak from the impurity phase was observed after 15 min of thermal annealing, indicating the
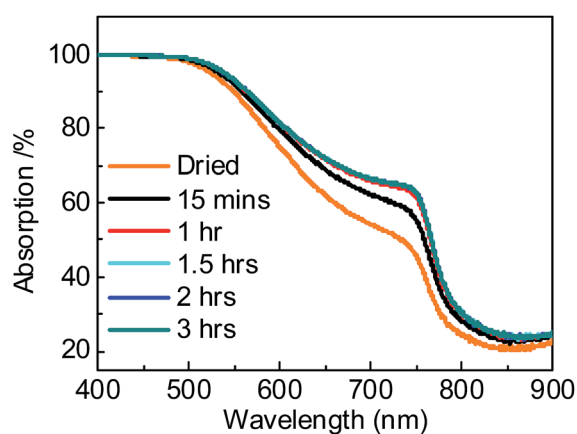
formation of a perovskite phase under 105 °C is efficient. After 3 h of thermal annealing, a small amount of PbI$_2$ phase showed up, which should originate from the decomposition of perovskite after long time annealing. All the annealed films have similar XRD patterns while the diffraction peaks become sharper with the increased annealing time. As illustrated in Fig. 3(b), the full width at half maximum (FWHM) of the (110) peak reduce gradually from 0.226° to 0.150° when the thermal annealing time increased from 15 min to 3 h. It should be noted that both increased crystallinity with less defects and a larger grain size with less grain boundaries can result in a sharper XRD peak. The increased crystalline grain size with thermal annealing was confirmed by the following SEM characterization. Also, the Hall effect and UPS measurement showed a decreased hole concentration with an increased annealing time, which indicates a reduced doping effect caused by the defects because point defects in MAPbI$_3$ work as dopants rather than generating trap states in the bandgap.[40,41] Thus, the sharper peak observed here should result from both enlarged grain size and increased crystallinity. In addition, it is observed that the intensity of the (110) diffraction peak at 16.69° increased gradually in the first 1.5 h of annealing, and then kept almost the same in the following 1.5 h, as shown in Fig. 3(c). Meanwhile, the relative intensity of the (110) diffraction peak to the (310) diffraction peak does not change significantly during thermal annealing, as shown in Fig. 3(c). Thus the increased (110) peak intensity should be caused by increased crystallinity rather than change in the crystal orientation.

3.3.   Scanning electron microscopy study

The increase of grain size in perovskite films upon thermal annealing was confirmed by the SEM study. The SEM images in Fig. 4(a) and (b) show the overall film morphology of the perovskite films after thermal annealing for 15 min or 3 h, respectively. The perovskite films grown on ITO/PEDOT:PSS by the interdiffusion method were continuous and compact even after 3 h of thermal annealing, which is in contrast to the discontinuous films fabricated from pre-mixed precursors.[27] Fig. 4(c)–(g) show the morphology change of the perovskite film during thermal annealing. The grain size distribution derived from these images is shown in Fig. 4(h). The average grain size increased with thermal annealing, consistent with the gradually decreased FWHM of XRD peaks in Fig. 3(b). After 15 min of thermal annealing the average gain size was 190 nm, and then it increased to around 350 nm and 380 nm after 2 h and 3 h annealing, respectively. The maximum grain size was 600–700 nm. It is noted that the grain size is comparable with or larger than the thickness of the film so that there is a minimized grain boundary in the charge collection direction of the annealed perovskite films, which contributes to a high efficiency in the perovskite solar cells.

3.4.   Hall effect measurement

In order to study the influence of thermal annealing on the carrier concentration and carrier mobility of the perovskite film, we conducted Hall effect measurement. The perovskite
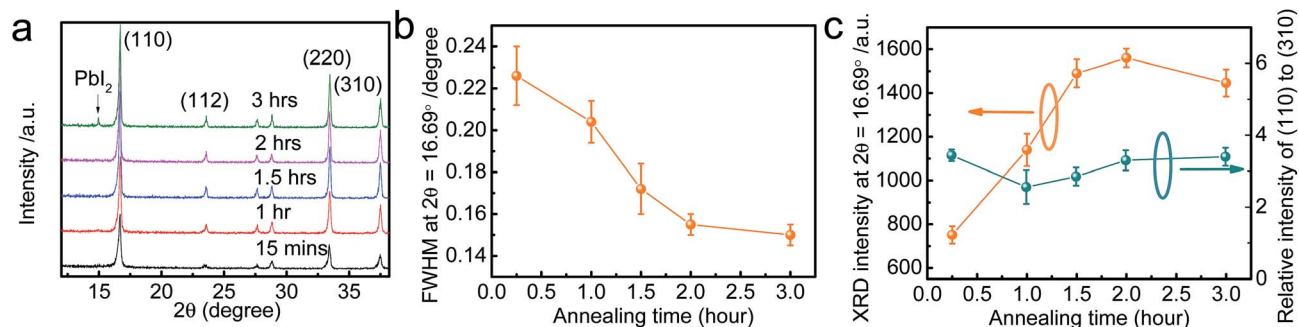

Fig. 2   Single path absorption spectra of MAPbI$_3$ perovskite films dried at 75 °C for 10 min and annealed at 105 °C for varied durations.

Fig. 3 (a) XRD patterns of MAPbI$_3$ perovskite films annealed at 105 °C for varied durations; (b) evolution of film's FWHM of the (110) diffraction peak with an increased annealing time; (c) variation of XRD peak intensity at $2\theta = 16.69°$ (left Y-axis) and its relative intensity to the (310) peak (right Y-axis) with an increased annealing time.
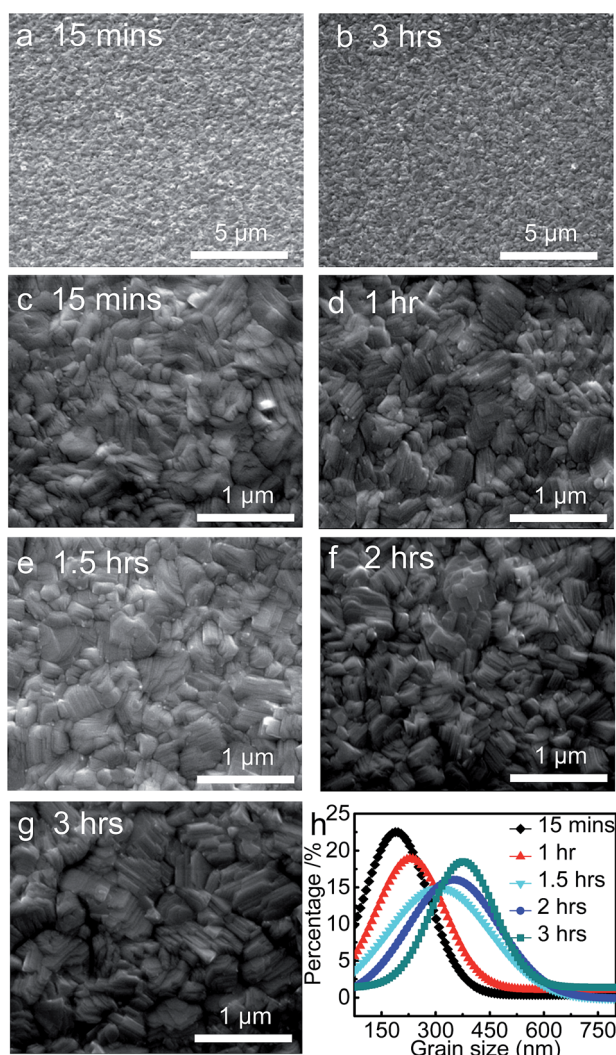

Fig. 4 (a and b) Morphology of MAPbI$_3$ perovksite films annealed at 105 °C for (a) 15 min, and (b) 3 h; (c−g) enlarged SEM images of MAPbI$_3$ films with different annealing times: (c) 15 min, (d) 1 h, (e) 1.5 h, (f) 2 h, and (g) 3 h; (h) grain size distribution of the films with varied annealing durations.

electronic properties are sensitive to the fabrication methods. All the films grown by the interdiffusion method showed p-type behaviour which is in contrast to the n-type perovskite formed from a pre-mixed perovskite precursor.[42,43] Recent calculation results on atomic defects in perovskites showed that Pb and MA vacancy acts as a p-type dopant and the I vacancy acts as a n-type dopant.[40,41] In the interdiffusion-grown perovskite films, a fixed amount of PbI$_2$ layer was prepared (150 nm), and then a relatively high concentration precursor solution (40 mg ml^{-1}) was used to deposit a MAI layer on the top of the PbI$_2$ layer,[44] which most likely resulted in point defects like Pb vacancies during the interdiffusion process and thus resulted in p-type perovskite films. Fig. 5 shows the variation of hole concentration and hole mobility with the annealing time. There is a clear increase of Hall mobility from 13.7 cm^2 V^{-1} s^{-1} to 28.7 cm^2 V^{-1} s^{-1}, accompanied by a reduction of the hole concentration from 5.9×10^{14} cm^{-3} to 2.7×10^{14} cm^{-3}, for films with an increased annealing time from 15 min to 1 h. It again indicates the formation of stoichiometric, phase pure, perovskite. The Hall mobility further increases from 28.7 cm^2 V^{-1} s^{-1} to 36.0 cm^2 V^{-1} s^{-1}, accompanied by the slight reduction of hole concentration from 2.7×10^{14} cm^{-3} to 2.4×10^{14} cm^{-3} with continued thermal annealing up to 3 h. This
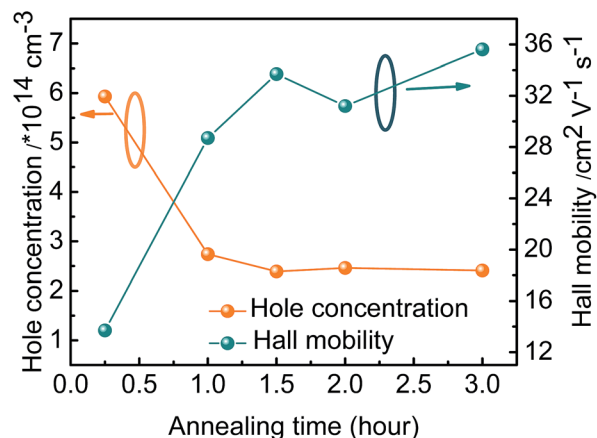

Fig. 5 Carrier concentration and Hall mobility of the perovskite films with varied annealing durations.

increased mobility correlates well with increased grain crystallinity and grain size in the perovskite films revealed by XRD and SEM measurements. The reduced hole concentration can be explained by fewer defects such as atomic vacancies, interstitial atoms or grain boundaries which can be a source of excess carriers. It is interesting to note that PbI_2 from slight decomposition at the third hour did not increase the hole concentration. This may result from the small amount of PbI_2 in grain boundaries which did not work as a dopant and was less likely to cause defects since PbI_2 has a larger bandgap (2.3 eV).[45]

3.5. Device's photovoltaic performance

The larger grains reduced the total grain boundary area, which is expected to reduce the charge recombination at the grain boundaries and improve device performance. The interdiffusion grown perovskite films with proper thermal annealing possess desired features for perovskite thin film photovoltaic applications, including full coverage on substrates, complete conversion of precursors, improved crystallinity and enlarged grain size. To investigate the annealing effect on the device performance, we fabricated devices with a structure of ITO/PEDOT:PSS (25 nm)/$MAPbI_3$ (280 nm)/PCBM (20 nm)/C_{60} (20 nm)/BCP (8 nm)/aluminium (100 nm). Here, the PCBM/C_{60} bilayer was applied on the top of the annealed perovskite film to passivate the surface defects on the perovskite film, which was found critical in achieving high efficiency devices.[33,36,43] Fig. 6(a) compares the J–V curves of the perovskite devices with different thermal annealing times at a temperature of 105 °C. The short-circuit current density (J_{SC}), open-circuit voltage (V_{OC}) and fill factor (FF) derived from J–V curves are summarized in Fig. 6(b). The J_{SC} increased from 14.9 mA cm^{-2} to 19.0 mA cm^{-2} after 2 h of thermal annealing. The FF also increased steadily from 69% to 78% after 2 h of thermal annealing and did not decrease in the following annealing process. A maximum PCE of 13.4% was obtained by annealing the perovskite films at 105 °C for 2 h due to the significantly increased FF and J_{SC}. The much increased FF and J_{SC} can be explained by the reduction of bulk trap density and increased carrier mobility, which originated from the increased perovskite stoichiometry, crystallinity and grain size. It is worth noting that the obtained perovskite device has a FF as large as 78%, which is larger than that of most perovskite photovoltaic devices with a planar heterojunction or mesoporous structure having a FF of 60–75%.[1–26] In addition, the shunt resistance increased from 1.51×10^4 ohm to over 3.71×10^4 ohm with a longer annealing time, as shown in Table 1. This should be attributed to the reduced carrier concentration, which gives a lower leakage in devices. Also, reduced series resistances were observed, which come from increased carrier mobility, improved interface and better crystallinity with fewer defects.

Nevertheless, the thermal annealing on the interdiffusion grown perovskite film led to a reduced V_{OC}, as shown in Fig. 6(b). Three hours of annealing pulled down the V_{OC} from 0.95 V to 0.88 V. Generally, an increased grain size leads to a larger V_{OC} because of the reduced charge recombination at grain boundaries, while the increased grain size with annealing
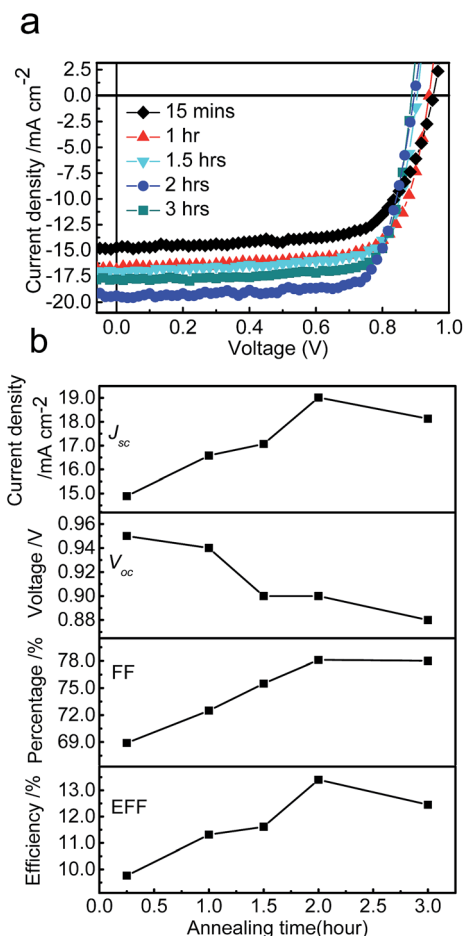
Fig. 6 Performance of the $MAPbI_3$ perovskite devices made of films after 105 °C annealing for different durations: (a) photocurrent density−voltage curves of the devices under simulated AM 1.5 irradiation (100 mW cm^{-2}); (b) variation of device parameters, J_{SC}, V_{OC}, FF and PCE, with increased annealing durations.

time observed in this work ruled out the grain boundary recombination as the dominating factor for the reduced V_{OC}. We noted that the hole concentration was reduced by thermal annealing. This reduction of the carrier concentration has a negative impact on V_{OC}. The V_{OC} of the photovoltaic device is ultimately determined by the quasi-Fermi energy level splitting of the electrons and holes under illumination:

$$V_{OC} = k_B T \ln \frac{(p + \Delta p)(n + \Delta n)}{n_i^2} \qquad (1)$$

where k_B, T, p, n, Δp, Δn, n_i^2 are the Boltzmann constant, temperature, hole concentration in the dark, electron

Table 1 Shunt and series resistances of the devices with perovskite films annealed after varied durations

Annealing time (h)	0.25	1	1.5	2	3
Series resistances (ohm cm^2)	5.46	3.49	1.67	1.78	1.43
Shunt resistances ($\times 10^4$ ohm)	1.51	1.68	2.57	3.83	3.71

18512 | J. Mater. Chem. A, 2014, 2, 18508–18514

This journal is © The Royal Society of Chemistry 2014

concentration in the dark, photogenerated hole concentration, electron concentration and intrinsic carrier concentration, respectively. Since our materials are p-type ($p \gg n$), and photons generated equal number of electrons and holes, the eqn (1) can be simplified as:

$$V_{OC} = k_B T \ln \frac{(p + \Delta p)\Delta p}{n_i^2} \qquad (2)$$

where Δp is a constant that is determined by the incident light intensity and by assuming that the charge generation efficiency is the same for all the films. Therefore a smaller hole concentration gives a reduced V_{OC} as is the case for perovskite solar cells reported here.

The reduced hole concentration in annealed perovskite films is also confirmed by the UPS study. The work function of the annealed perovskite films gradually reduced from 5.21 eV to 5.08 eV with the increased annealing time. It should be noted that the work function of the perovskite films formed by interdiffusion is much different from those formed from premixed precursors.[46] A reduced work function lifts the Fermi energy toward the middle of the bandgap, yielding a smaller hole concentration as measured, as shown in Fig. 7(a). It shows that annealing is a method to control the work function and even doping concentration in interdiffusion-grown perovskite films. Since the hole concentration is exponentially dependent on both the shift of Fermi energy level and the V_{OC}, it is expected that there is a linear relationship between the work function and V_{OC}. Fig. 7(b) shows the plot of V_{OC} and work function in the same figure with a shifted V_{OC}. A clear linear correlation

between them was observed for the devices with an annealing time less than two hours. The discrepancy for the three hour annealing sample might be caused by the decomposition of the perovskite films, yielding a larger V_{OC} than that predicted from the Fermi energy shift. The results shown here point out that a future direction to increase the device efficiency is to slightly increase the carrier concentration of the perovskite layer without causing significant charge recombination.

4. Conclusions

The interdiffusion method for fabricating a perovskite solar cell provides a low cost and feasible solution to achieve high performance due to the formation of continuous absorber films with full surface coverage. By understanding the thermal annealing effect on perovskite films, we demonstrated that the crystallinity and grain size is critical to optimize the device performance. The increased annealing time at a relatively low temperature (105 °C) improved the device performance overall by increasing J_{SC} and FF. The highest PCE of 13.4% was achieved when the perovskite absorber layer was treated by 2 h of thermal annealing at 105 °C. In addition, it is expected that the annealing process can optimize the performance of perovskite solar cells with mesoporous architecture or formed from blending precursors.

Notes and references

1 P. Docampo, J. M. Ball, M. Darwich, G. E. Eperon and H. J. Snaith, *Nat. Commun.*, 2013, **4**, 2761.

2 C. H. Lee, D. R. Kim, I. S. Cho, N. William, Q. Wang and X. Zheng, *Sci. Rep.*, 2012, **2**, 1000.

3 V. Shrotriya, *Nat. Photonics*, 2009, **3**, 447–449.

4 W. Ma, C. Yang, X. Gong, K. Lee and A. J. Heeger, *Adv. Funct. Mater.*, 2005, **15**, 1617–1622.

5 J. A. Mikroyannidis, A. N. Kabanakis, S. S. Sharma and G. D. Sharma, *Adv. Funct. Mater.*, 2011, **21**, 746–755.

6 F. Liu, Y. Gu, J. W. Jung, W. H. Jo and T. P. Russell, *J. Polym. Sci., Part B: Polym. Phys.*, 2012, **50**, 1018–1044.

7 J. Jo, S.-S. Kim, S.-I. Na, B.-K. Yu and D.-Y. Kim, *Adv. Funct. Mater.*, 2009, **19**, 866–874.

8 T. M. Clarke, A. M. Ballantyne, J. Nelson, D. D. C. Bradley and J. R. Durrant, *Adv. Funct. Mater.*, 2008, **18**, 4029–4035.

9 M.-G. Tsai, H.-T. Tung, I.-G. Chen, C.-C. Chen, Y.-F. Wu, X. Qi, Y. Hwu, C.-Y. Lin, P.-H. Wu and C.-W. Cheng, *J. Am. Ceram. Soc.*, 2013, **96**, 2419–2423.

10 S. Niki, M. Contreras, I. Repins, M. Powalla, K. Kushiya, S. Ishizuka and K. Matsubara, *Prog. Photovolt. Res. Appl.*, 2010, **18**, 453–466.

11 C.-J. Hsu, H.-S. Duan, W. Yang, H. Zhou and Y. Yang, *Adv. Energy Mater.*, 2013, **4**, 1301287.

12 S. Engmann, C. R. Singh, V. Turkovic, H. Hoppe and G. Gobsch, *Adv. Energy Mater.*, 2013, **3**, 1463–1472.

13 F. Padinger, R. S. Rittberger and N. S. Sariciftci, *Adv. Funct. Mater.*, 2003, **13**, 85–88.

14 C. J. Brabec, S. Gowrisanker, J. J. M. Halls, D. Laird, S. Jia and S. P. Williams, *Adv. Mater.*, 2010, **22**, 3839–3856.
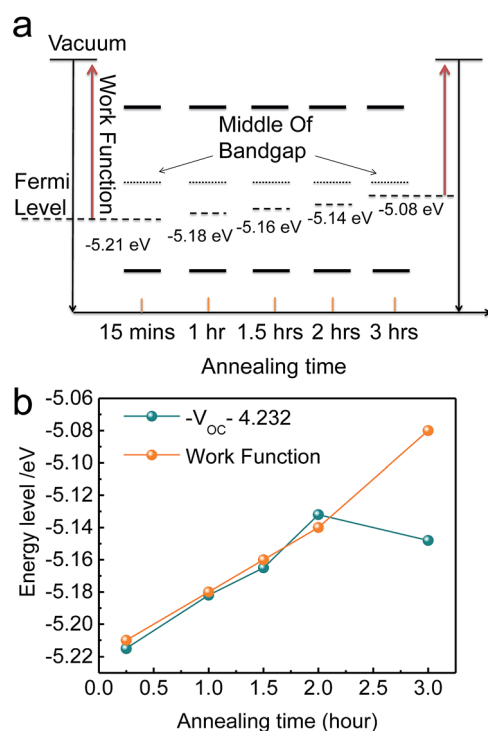
Fig. 7 (a) Energy diagram of Fermi energy shifting during thermal annealing; (b) MAPbI$_3$ perovskite film work function and V_{OC} of the corresponding devices with increased annealing durations.

This journal is © The Royal Society of Chemistry 2014

J. Mater. Chem. A, 2014, **2**, 18508–18514 | **18513**

15 M. Bodeg Ård, K. Granath and L. Stolt, *Thin Solid Films*, 2000, **361–362**, 9–16.

16 L. Kronik, D. Cahen and H. W. Schock, *Adv. Mater.*, 1998, **10**, 31–36.

17 M. Venkatachalam, M. D. Kannan, S. Jayakumar, R. Balasundaraprabhu and N. Muthukumarasamy, *Thin Solid Films*, 2008, **516**, 6848–6852.

18 M. Krunks, O. Kijatkina, H. Rebane, I. Oja, V. Mikli and A. Mere, *Thin Solid Films*, 2002, **403–404**, 71–75.

19 M. Kaelin, D. Rudmann, F. Kurdesau, T. Meyer, H. Zogg and A. N. Tiwari, *Thin Solid Films*, 2003, **431–432**, 58–62.

20 B. Bob, B. Lei, C.-H. Chung, W. Yang, W.-C. Hsu, H.-S. Duan, W. W.-J. Hou, S.-H. Li and Y. Yang, *Adv. Energy Mater.*, 2012, **2**, 504–522.

21 K. Wojciechowski, M. Saliba, T. Leijtens, A. Abate and H. J. Snaith, *Energy Environ. Sci.*, 2014, **7**, 1142–1147.

22 H.-S. Kim, C.-R. Lee, J.-H. Im, K.-B. Lee, T. Moehl, A. Marchioro, S.-J. Moon, R. Humphry-Baker, J.-H. Yum, J. E. Moser, M. Gratzel and N.-G. Park, *Sci. Rep.*, 2012, **2**, 591.

23 J. Burschka, N. Pellet, S.-J. Moon, R. Humphry-Baker, P. Gao, M. K. Nazeeruddin and M. Gratzel, *Nature*, 2013, **499**, 316–319.

24 D. Liu and T. L. Kelly, *Nat. Photonics*, 2014, **8**, 133–138.

25 M. Liu, M. B. Johnston and H. J. Snaith, *Nature*, 2013, **501**, 395–398.

26 O. Malinkiewicz, A. Yella, Y. H. Lee, G. M. Espallargas, M. Graetzel, M. K. Nazeeruddin and H. J. Bolink, *Nat. Photonics*, 2014, **8**, 128–132.

27 G. E. Eperon, V. M. Burlakov, P. Docampo, A. Goriely and H. J. Snaith, *Adv. Funct. Mater.*, 2014, **24**, 151–157.

28 A. Dualeh, N. Tétreault, T. Moehl, P. Gao, M. K. Nazeeruddin and M. Grätzel, *Adv. Funct. Mater.*, 2014, **24**, 3250–3258.

29 S. D. Stranks, G. E. Eperon, G. Grancini, C. Menelaou, M. J. P. Alcocer, T. Leijtens, L. M. Herz, A. Petrozza and H. J. Snaith, *Science*, 2013, **342**, 341–344.

30 Q. Chen, H. Zhou, Z. Hong, S. Luo, H.-S. Duan, H.-H. Wang, Y. Liu, G. Li and Y. Yang, *J. Am. Chem. Soc.*, 2014, **136**, 622–625.

31 N. J. Jeon, J. H. Noh, Y. C. Kim, W. S. Yang, S. Ryu and S. I. Seok, *Nat. Mater.*, 2014, **13**, 897–903.

32 H. Zhou, Q. Chen, G. Li, S. Luo, T.-B. Song, H.-S. Duan, Z. Hong, J. You, Y. Liu and Y. Yang, *Science*, 2014, **345**, 542–546.

33 T. Leijtens, G. E. Eperon, S. Pathak, A. Abate, M. M. Lee and H. J. Snaith, *Nat. Commun.*, 2013, **4**, 2885.

34 J.-Y. Jeng, Y.-F. Chiang, M.-H. Lee, S.-R. Peng, T.-F. Guo, P. Chen and T.-C. Wen, *Adv. Mater.*, 2013, **25**, 3727–3732.

35 J. You, Z. Hong, Y. M. Yang, Q. Chen, M. Cai, T.-B. Song, C.-C. Chen, S. Lu, Y. Liu, H. Zhou and Y. Yang, *ACS Nano*, 2014, **8**, 1674–1678.

36 Z. Xiao, C. Bi, Y. Shao, Q. Dong, Y. Yuan, C. Wang, Y. Gao and J. Huang, *Energy Environ. Sci.*, 2014, **7**, 2619–2623.

37 M. M. Lee, J. Teuscher, T. Miyasaka, T. N. Murakami and H. J. Snaith, *Science*, 2012, **338**, 643–647.

38 Q. Chen, H. Zhou, T.-B. Song, S. Luo, Z. Hong, H.-S. Duan, L. Dou, Y. Liu and Y. Yang, *Nano Lett.*, 2014, **14**, 4158–4163.

39 Y. Zhao and K. Zhu, *J. Phys. Chem. Lett.*, 2013, **4**, 2880–2884.

40 W.-J. Yin, T. Shi and Y. Yan, *Appl. Phys. Lett.*, 2014, **104**, 063903.

41 J. Kim, S.-H. Lee, J. H. Lee and K.-H. Hong, *J. Phys. Chem. Lett.*, 2014, **5**, 1312–1317.

42 B. Conings, L. Baeten, C. De Dobbelaere, J. D'Haen, J. Manca and H.-G. Boyen, *Adv. Mater.*, 2014, **26**, 2041–2046.

43 Q. Wang, Q. Dong, Z. Xiao, Y. Yuan and J. Huang, *Energy Environ. Sci.*, 2014, **7**, 2359–2365.

44 Q. Wang, Y. Shao, H. Xie, L. Lyu, X. Liu, Y. Gao and J. Huang, *Appl. Phys. Lett.*, 2014, submitted.

45 Q. Chen, H. Zhou, T.-B. Song, S. Luo, Z. Hong, H.-S. Duan, L. Dou, Y. Liu and Y. Yang, *Nano Lett.*, 2014, **14**, 4158–4163.

46 P. Schulz, E. Edri, S. Kirmayer, G. Hodes, D. Cahen and A. Kahn, *Energy Environ. Sci.*, 2014, **7**, 1377–1381.